Closed forms for spatiotemporal optical vortices and sagittal skyrmionic pulses

OPEN ACCESS
IOP Publishing
Journal of Optics
J. Opt. **26** (2024) 095607 (12pp)
https://doi.org/10.1088/2040-8986/ad6a26

Closed forms for spatiotemporal optical vortices and sagittal skyrmionic pulses

S Vo[1], R Gutiérrez-Cuevas[2] and M A Alonso[1,3,4,*]

[1] The Institute of Optics, University of Rochester, Rochester, NY 14627, United States of America
[2] Institut Langevin, ESPCI Paris, Université PSL, CNRS, 75005 Paris, France
[3] Aix Marseille Univ, CNRS, Centrale Med, Institut Fresnel, UMR 7249, Marseille Cedex 20, 13397, France
[4] Laboratory for Laser Energetics, University of Rochester, Rochester, NY 14627, United States of America

E-mail: miguel.alonso@fresnel.fr

Received 4 June 2024, revised 26 July 2024
Accepted for publication 1 August 2024
Published 12 August 2024

Abstract

Spatiotemporal optical vortices (STOVs) are short pulses that present a vortex whose axis is perpendicular to the main propagation direction. We present analytic expressions for these pulses that satisfy exactly Maxwell's equation, by applying appropriate differential operators to complex focus pulses with Poisson-like frequency spectrum. We also provide a simple ray picture for understanding the deformation of these pulses under propagation. Finally, we use these solutions to propose a type of pulse with sagittal skyrmionic polarization distribution covering all states of transverse polarization.

Keywords: structured light, spatiotemporal optical vortices, skyrmions

1. Introduction

A broad range of short light pulses with interesting distributions in space and time have been studied theoretically and implemented experimentally. For a description of many of these pulses, the reader can consult extensive reviews of this topic [1–3]. From the theoretical point of view, only a small subset of these pulses can be expressed as closed-form solutions of Maxwell's equations. One such case is that of donut-shaped (or toroidal) pulses that present rotational symmetry about the main direction of propagation, and include a nodal line along this axis of symmetry [4–6]. Recently, a different kind of donut-shaped pulse, referred to as spatiotemporal optical vortex (STOV), has received significant attention [7–22]. Unlike the toroidal pulses mentioned earlier, STOVs present the peculiarity of carrying a phase vortex whose axis is perpendicular to their main direction of propagation, hence resembling advancing hurricanes or cyclones. Closed-form expressions for STOVs have been proposed only within the paraxial approximation [14, 19]. In particular, Porras [19] derived an expression for a paraxial STOV involving a Hermite polynomial evaluated at a complex argument, hence providing a spatiotemporal analog of what is known as generalized (or Hermite–Laguerre–)Gaussian beams [23, 24]. To our knowledge, no closed-form expression valid beyond the paraxial regime has been proposed for STOVs.

The current work has several goals:

The first is to propose a relatively simple closed-form expression for representing STOVs, both for scalar and electromagnetic (vector) fields, which are exact solutions of the wave or Maxwell equations in free space, and are then valid beyond the paraxial regime. Using this theoretical model, we find conditions to make these vortices as isotropic as possible at the focal time. The key to finding these solutions is the use of the complex focus model [25–27] which consists

* Author to whom any correspondence should be addressed.

on assigning complex spatial coordinates to the focal point of a monochromatic spherical wave. This method has been used, for example, to construct bases for describing highly focused electromagnetic fields [28–30] which, in turn, simplify the description of Mie scattering [31, 32]. The complex focus method can be extended to the study of time-dependent pulsed electromagnetic fields by integrating these monochromatic solutions weighted by a given frequency spectrum [33–38]. In particular, a Poisson-like spectrum leads to a closed-form expression and allows identifying the resulting complex fields as the analytic signal representation of the real fields [39, 40].

The second goal is to provide an intuitive explanation to the asymmetric deformation that these pulses experience as they propagate. While these deformations are naturally incorporated into closed-form expressions, they can be better understood by using a simple ray-based model that is compatible with the complex-focus picture.

The third and final goal of this work is to use these models to propose a new type of electromagnetic pulse that presents over its sagittal plane a 'Stokes-skyrmionic' distribution of polarization, in which all paraxial states of full polarization are represented. This pulse is motivated by recent interest in optical fields presenting skyrmonic structures, which are localized regions where a field property, such as paraxial polarization or the spin of nonparaxial vector electric fields, covers the surface of a sphere [41–47]. However, unlike for the simple case of full Poincaré beams [42, 46, 48] where this structure is present over transverse planes, the pulsed fields described here cover the Poincaré sphere over sagittal planes parallel to the propagation axis.

2. The fundamental scalar pulsed field

Monochromatic complex focus fields were proposed as exact closed-form singularity-free solutions to the Helmholtz equation $\nabla^2 U + (\omega/c)^2 U = 0$ (where ω is the frequency and c is the speed of light in vacuum) that generalize Gaussian beams into the nonparaxial regime [25–27]. They take the form of a standing spherical wave focused at a complex position according to

$$U(\boldsymbol{r},\omega) = 2\mathrm{i}c \exp\left(-\frac{\omega|\boldsymbol{q}|}{c}\right) U_0(\omega) \frac{\sin\left(\frac{\omega}{c}R\right)}{\omega R}, \qquad (1)$$

where $U_0(\omega)$ is an amplitude factor (written here as a function of frequency in anticipation of a derivation that follows) and $R = [(\boldsymbol{r}-\boldsymbol{\rho}_0)\cdot(\boldsymbol{r}-\boldsymbol{\rho}_0)]^{1/2}$ is the complex distance between the observation point $\boldsymbol{r}$ and the complex coordinate $\boldsymbol{\rho}_0 = \boldsymbol{r}_0 + \mathrm{i}\boldsymbol{q}$, with $\boldsymbol{r}_0$ being the focal point and $\boldsymbol{q}$ determining the directionality of the field. We also include a damping factor $\exp(-\omega|\boldsymbol{q}|/c)$ to guarantee convergence [38]. For a field whose main direction of propagation is aligned with the positive z axis, $\boldsymbol{q}$ can be written as $q\hat{\boldsymbol{z}}$ with $q>0$ and where $\hat{\boldsymbol{z}}$ is the unit vector in the z direction. For $\omega q/c \gg 1$, the field tends towards a Gaussian beam whose Rayleigh range is q. For simplicity we place the focal point $\boldsymbol{r}_0$ at the origin, so that we can write $R = \sqrt{x^2+y^2+(z-\mathrm{i}q)^2}$.

Pulsed beams with closed-form solutions can also be constructed by using the concept of complex focus [38]. The key is to integrate over frequency the product of $\exp(-\mathrm{i}\omega t)$ and the monochromatic complex focus solution in equation (1) with q (the Rayleigh range) being the same for all frequencies. This condition leads to isodiffracting pulses [40, 49, 50] and is used to model pulses generated inside cavities where the Rayleigh range is determined by the geometry of the cavity and is independent of the frequency. By writing $U_0(\omega) = \omega A(\omega)$, the result is expressible in terms of the inverse Fourier transform of $A(\omega)$. One simple option would then be to choose A as a Gaussian centered at a frequency ω_0. One minor issue with this choice, though, is that the simple result would involve some amount of negative frequency contributions. This is not a problem if all we require is a closed form for the real field. However, sometimes it is convenient to have a form for the complex analytic signal representation of the field, e.g. to calculate easily short-time-average intensities or Poynting vectors. It is then better to use a spectrum that allows a simple closed-form solution even when integrating only over positive frequencies. A frequency spectrum following a Poisson-like distribution satisfies these properties [40] and therefore will be used:

$$U_0(\omega) = \left(\frac{s}{\omega_0}\right)^{s+1} \frac{\omega^s \exp\left(-\frac{s\omega}{\omega_0}\right)}{\Gamma(s+1)} \Theta(\omega), \qquad (2)$$

where $\Theta(\cdot)$ is the Heaviside distribution that ensures that only positive frequencies are involved, ω_0 is the peak frequency, and s controls the width of the spectrum and thus the pulse duration. It is shown in appendix A that the resulting field is simply given by

$$E(\boldsymbol{r},t) = \frac{1}{\omega_0 R}\left[\frac{1}{\left(1+\mathrm{i}\frac{\omega_0}{s}t_-\right)^s} - \frac{1}{\left(1+\mathrm{i}\frac{\omega_0}{s}t_+\right)^s}\right], \qquad (3)$$

where $t_\pm = t \pm R/c - \mathrm{i}q/c$. The actual field corresponds to the real part of the complex function in equation (3). However, this complex expression facilitates the computation of what we call the short-time averaged intensity as $|E|^2$, which corresponds approximately to the intensity averaged over an optical cycle.

Figure 1 shows the short-time-averaged intensity of the resulting pulse for various values of q. These plots also show the dependence of the spatial dimensions of the pulse on the parameters q and s. As q changes for fixed s, the longitudinal size of the pulse stays constant while the transverse size varies. Therefore, the pulse's width (and level of collimation) is controlled by q, while its length (and duration) is determined by s. As shown in appendix B, by considering the short-time averaged intensity for $t=0$, the transverse extension of the pulse is approximately given by the standard expression in terms of the Rayleigh range q, namely $\sqrt{q/k_0}$, where $k_0 = \omega_0/c$. The longitudinal extension of the pulse, on the other hand, is roughly

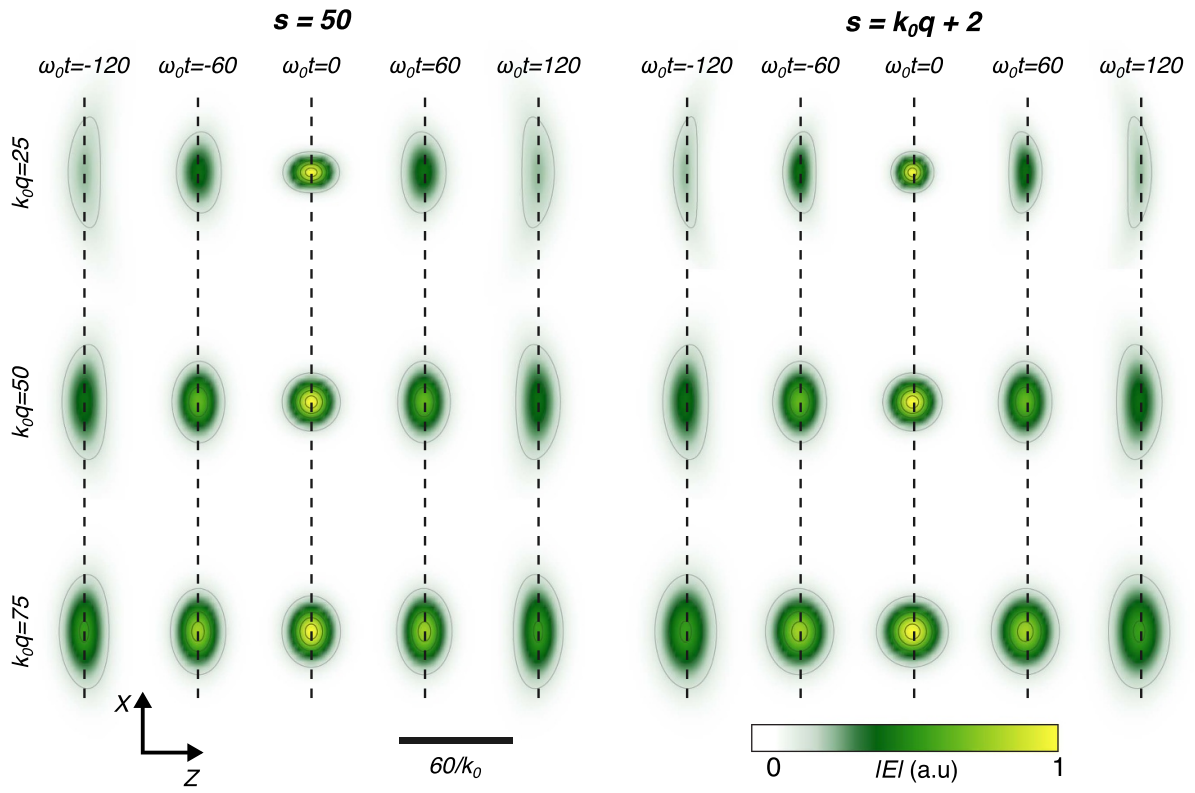

Figure 1. Short-time averaged intensity of a round pulse at five equally spaced times centered at $t=0$ indicated in units of $1/\omega_0$, for increasing values of q from top to bottom. For the plots on the left side $s=50$, whereas for the plots on the right side $s=k_0q+2$.

proportional to $\sqrt{s}/k_0$. The condition for making the pulse round is then found to be given approximately by

$$s = k_0 q + 2, \tag{4}$$

valid for k_0q sufficiently greater than unity. Note that pulses approaching the paraxial condition have Rayleigh ranges that are much larger than the wavelength for the central frequency, so that the first term dominates, and the second can be neglected. We do keep the second term of equation (4) as a first correction to the roundness of the packet in the nonparaxial regime. The width of the pulse at $t=0$ in any direction is then given approximately by $\sqrt{q/k_0}$. Figure 1 shows the short-time-averaged intensity of the resulting round pulse at five times around $t=0$, for increasing values of q from top to bottom.

3. Scalar STOV

The expression for the round blob pulse just described can be turned into one representing a STOV that carries transverse orbital angular momentum (OAM) by applying an appropriate differential operator. By choosing the OAM to point in the y direction, the differential operator is constructed as

$$\widehat{W} = \frac{1}{k_0}\partial_x \pm \mathrm{i}\left(\frac{\alpha}{\omega_0}\partial_t + \frac{\beta}{k_0}\partial_z + \mathrm{i}\gamma\right), \tag{5}$$

where α, β, and γ are constant parameters to be determined. The justification for this operator is the following: the derivative in x on its own introduces a nodal plane at $x=0$ given the symmetry of the original pulse, while the combination in parentheses on its own introduces a nodal surface that is normal to the z axis. The constant coefficients α, β and γ can then be chosen so that at $t=0$ the pulse's short-time average intensity is symmetric around $z=0$ and as round as possible. These conditions are investigated in appendix C, where the following approximate results are found:

$$\alpha \approx \frac{2}{3} - \frac{26}{9s}, \qquad \beta \approx \frac{5}{3} - \frac{32}{9s}, \qquad \gamma \approx -1 + \frac{7}{3s}. \tag{6}$$

Note that we included a first nonparaxial correction in each of these coefficients, expressed in terms of the inverse of the dimensionless parameter $s=k_0q+2$ (assumed to be considerably larger than unity). The scalar STOV is then simply constructed as

$$E_{\mathrm{STOV}}(\boldsymbol{r},t) = \widehat{W}E(\boldsymbol{r},t). \tag{7}$$

Figure 2 shows the short-time averaged intensity and the real amplitude of these scalar STOVs for different values of q. As desired, these intensity distributions are approximately circular at $t=0$. While it is not the goal of the current work, we note that a STOV that is circular (or elliptical) over the (x,z) plane at $t=0$ is not so over a spatiotemporal plane (x,ct) at $z=0$, or conversely; according to Porras [21], these different criteria for defining STOVs are related to the discrepancies in the calculation of the OAM they carry [9, 14, 20, 22].

Note that the operator in equation (7) could be applied repeatedly to generate higher order STOVs. However, it turns

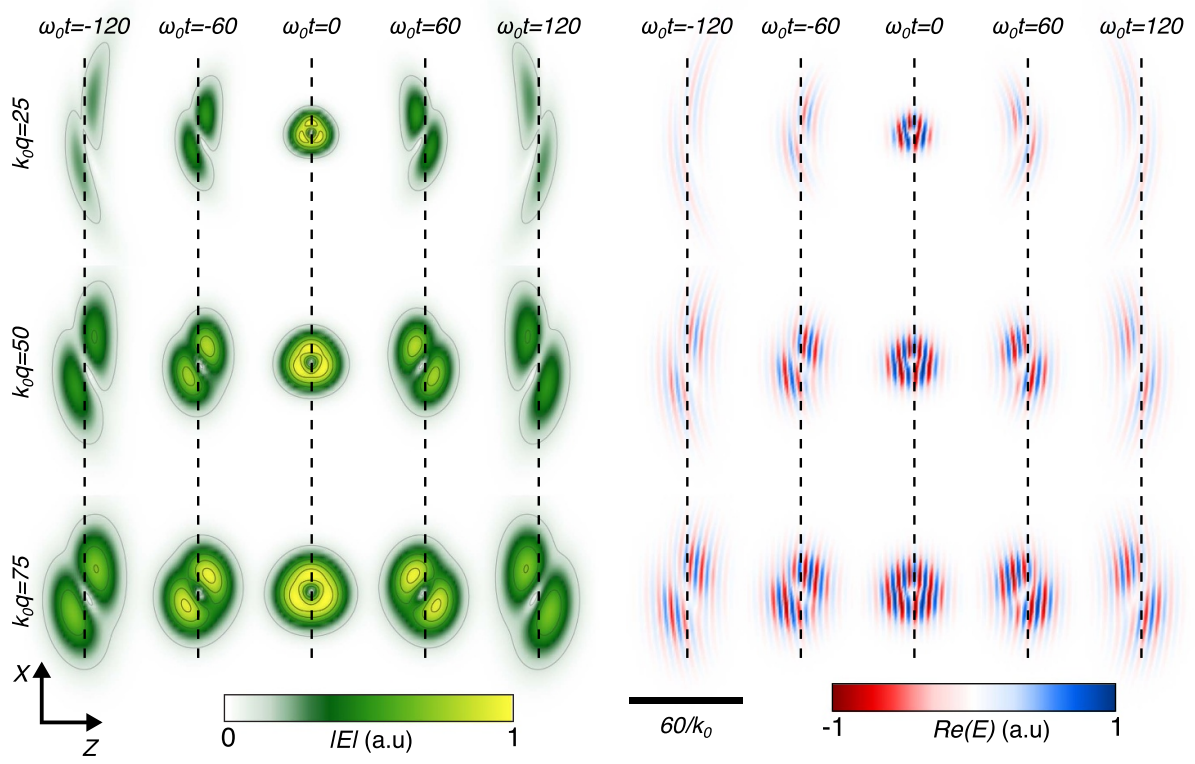

Figure 2. Short-time averaged intensity (left) and real amplitude (right) for scalar STOVs at five equally spaced times centered at $t=0$ indicated in units of $1/\omega_0$, for values of $k_0q=25,50,$ and 75 and $s=k_0q+2$.

out that even at $t=0$ this repeated application of the operator will not give a single higher order vortex at the center but a number of nearby vortices with equal unit charges. Engineering a round solution with a higher order vortex at $t=0$ would require considering an operator involving a linear combination of derivatives in x, z and t up to the desired order, and adjusting appropriately the constant coefficients for each term. Also, by including terms including derivatives in y, together with an appropriate adjustment of the constant coefficients, one could introduce a vortex whose axes are in any desired direction [18, 22].

4. Ray picture

One can understand the deformation of the STOV away from $t=0$ by using a simple ray picture in two dimensions. Consider a family of rays that are perfectly focused at an on-axis point $(x,z)=(0,z_0)$ and that have maximum slope τ. If we parametrize each ray in terms of a parameter ξ, the transverse x coordinate of these rays in terms of z can be written as

$$X(z,\xi)=(z-z_0)\,\tau\cos\xi=\tau\,\Re\left[(z-z_0)\exp(\mathrm{i}\xi)\right]. \quad (8)$$

If we now let z_0 become purely imaginary by substituting $z_0=\mathrm{i}q$, this equation becomes

$$X(z,\xi)=\tau\,\Re\left[(z-\mathrm{i}q)\exp(\mathrm{i}\xi)\right]=q\tau\sin\xi+z\tau\cos\xi. \quad (9)$$

This family of rays resembles a lateral projection of a ruled hyperboloid, and presents a hyperbolic caustic composed of two branches with vertices at $(x,z)=(\pm q\tau,0)$. This hyperbolic profile is consistent with the fact that, in the paraxial regime, Gaussian beams and their related modes such as Hermite- and Laguerre–Gaussian beams are associated often with families of rays described by a caustic that expands hyperbolically [51, 52], and that in the nonparaxial regime complex focused fields are connected with oblate spheroidal coordinates [36, 53].

To now mimic the behavior of a STOV, we consider a set of 'particles', each traveling along a ray at the same speed (the speed of light). The initial conditions for these particles are such that they trace at $t=0$ a circle of radius w centered at the origin. Note that two rays cross each point along this circle, so care must be taken in assigning which of these rays corresponds to the path of each particle. We can choose, for example, the rays with negative (positive) slope for all the points for which the particle is at $z>0$ ($z<0$) at $t=0$, as shown in figure 3, where the particles and their trajectories are identified by using different colors. This situation corresponds to OAM in the negative y direction (into the page), since the evolution of the loop formed by the particles implies a clockwise rotation. Notice that, in addition to this rotation and the global displacement to the right, the loop gets deformed with propagation, with the bottom part moving ahead of the top part. We also observe bunching near the two caustics.

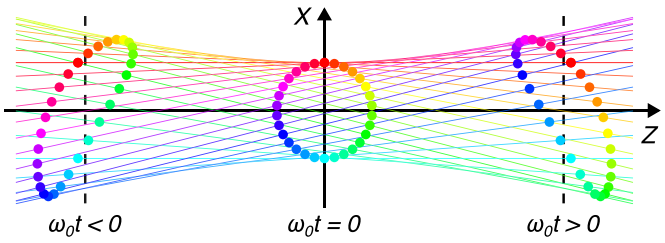

Figure 3. Ray-based picture for the deformation of a STOV with propagation. The STOV is represented as a set of particles (color dots) that form a circle at $t = 0$. All particles travel at the same speed (c), each along a different ray (shown in the same color as the corresponding particle). The picture shows also the deformed configuration of these particles at a later time.

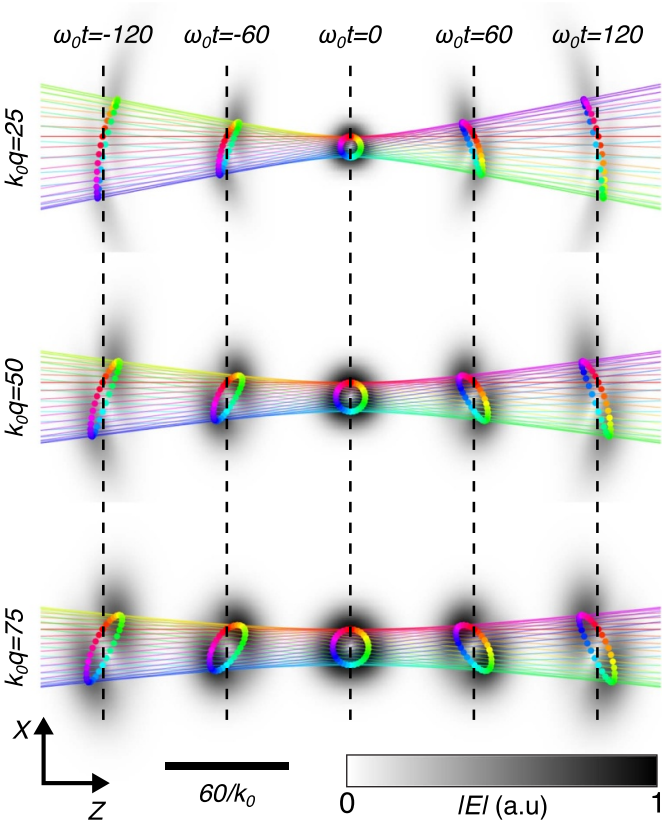

Figure 4. Superposition of ray/particle picture of STOV deformation under propagation to the short-time-averaged intensity of scalar STOVs at several times, and for values of $k_0 q = 25, 50,$ and 75, with $s = k_0 q + 2$.

Figure 4 shows the superposition of such sets of rays and particles on the short-time averaged intensity plots of round STOVs, with width $q\tau = \sqrt{q/k_0}$, that is, $\tau = 1/\sqrt{k_0 q}$. Notice that the particle distribution resembles the STOV's intensity maxima, and this correspondence improves as we approach the paraxial regime (i.e. for sufficiently large q). Note also that the particle distribution undergoes a sort of rotation with time around its centroid: the particles at the top and bottom of the loop correspond to rays that touch the caustics near the region of the loop. This rotation echoes the orbital angular momentum carried by the STOV.

5. Electromagnetic STOV

We now apply similar techniques in order to generate closed-form expressions for electromagnetic STOV. Scalar solutions can be transformed into vector ones by using operators based on the Hertz potential formalism. Here, we choose to use a time-domain version of operators that are particularly appropriate for fields propagating mostly in the positive z direction [54, 55]. This operator is given by

$$\widehat{\mathbf{V}}_{\boldsymbol{p}} = c^2 (\boldsymbol{p} \cdot \nabla) \nabla + c \partial_t (\hat{\boldsymbol{z}} \times \boldsymbol{p}) \times \nabla - \boldsymbol{p} \partial_t^2, \qquad (10)$$

where $\boldsymbol{p}$ is a dimensionless constant vector. This vector can be real or complex, and its transverse components correspond approximately to the polarization of the pulse near the z axis away from the focal region. For simplicity we then choose $\boldsymbol{p}$ to be constrained to the xy plane. For example, choosing $\boldsymbol{p} \propto (1, \pm \mathrm{i}, 0)$ leads to STOVs with definite helicity. The operator in equation (10) commutes with the D'Alembert (wave) operator and its divergence vanishes, so when applied to a scalar solution of the free-space wave equation it gives a vector form of the electric field that is fully consistent with Maxwell's equations. It is designed such that, when applied to a scalar pulse traveling in the positive z direction close to the paraxial regime and whose spectrum is not too broadly distributed around a central frequency ω_0, the resulting vector solution resembles the scalar field times $\omega_0^2 \boldsymbol{p}$.

Closed-form vector solutions for STOVs can be constructed by applying this operator to the scalar STOVs described in the previous section:

$$\mathbf{E}_{\mathrm{STOV}} (\boldsymbol{r}, t; \boldsymbol{p}) = \frac{1}{\omega_0^2} \widehat{\mathbf{V}}_{\boldsymbol{p}} \widehat{W} E (\boldsymbol{r}, t) . \qquad (11)$$

The operators $\widehat{\mathbf{V}}_{\boldsymbol{p}}$ and $\widehat{W}$ commute, so their order is not important. However, the application of the operator $\widehat{\mathbf{V}}_{\boldsymbol{p}}$ not only imparts a vectorial character to the field, but also causes some changes to its intensity profile, and hence deforms the STOV. As shown in appendix D, the approximate rotational symmetry of the STOV can be partially restored by adjusting the parameters within $\widehat{W}$ to slightly different values from those that achieve a round scalar STOV:

$$\alpha \approx \frac{6}{7}, \qquad \beta \approx \frac{13}{7} - \frac{237}{98 s}, \qquad \gamma \approx -1 + \frac{237}{98 s}. \qquad (12)$$

Figure 5 shows the short-time averaged intensity (the squared norm of the complex electric field) for these electromagnetic STOVs for several values of s from top to bottom and at different times, with $\boldsymbol{p} \propto (1, \mathrm{i}, 0)$. Note that, at the focal time, these pulses have a fairly round profile with a small trigonal deformation. In fact, as shown in appendix D, achieving this level of roundness also requires allowing the STOV to shift laterally by an amount $x_0 = \mp \lambda_0 / 14\pi$. This shift of a fraction of a wavelength can be regarded as a spin–orbit effect, similar to other spin-induced transverse shifts in optical beams [56–58].

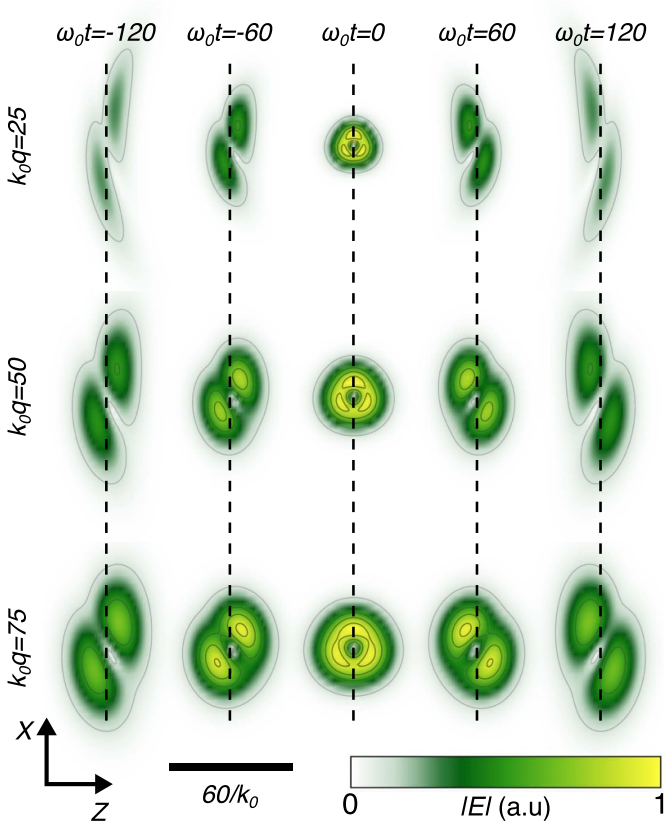

Figure 5. Short-time averaged intensity for electromagnetic STOVs with definite helicity, at five equally spaced times centered at $t=0$ indicated in units of $1/\omega_0$, and for values of $k_0 q = 25, 50$, and 75 and $s = k_0 q + 2$.

6. Paraxial limit

We now study the paraxial limit of the solutions discussed in the previous sections. The starting point is the paraxial form of the pulse in equation (3), which is found in appendix E to be given by

$$E(\boldsymbol{r},t) \approx \frac{1}{z-\mathrm{i}q}\exp\left\{\mathrm{i}k_0\left[z-ct+\frac{\rho^2}{2(z-\mathrm{i}q)}\right]\right\} \times \exp\left\{-\frac{k_0}{2q}\left[z-ct+\frac{\rho^2}{2(z-\mathrm{i}q)}\right]^2\right\}. \tag{13}$$

This expression is valid for $s \approx k_0 q \gg 1$. Notice that the first line corresponds to a monochromatic Gaussian beam of frequency ω_0, and the exponential factor in the second line is responsible for the longitudinal localization and the curvature of the intensity profile away from the focal region.

To find the corresponding formula for the scalar STOV we apply the operator in equation (5) to this paraxial pulse, using either the coefficients in equation (6) or those in equation (12). In both cases, the result is proportional to the pulse itself times a factor corresponding to a ratio of polynomials involving powers of $k_0 q$. By keeping only the leading terms in this factor for $k_0 q \gg 1$ we find the same result for both sets of coefficients:

$$E_{\mathrm{STOV}}(\boldsymbol{r},t) \approx \frac{q^2\left[\pm(ct-z)-\mathrm{i}x\right]}{(q+\mathrm{i}z)^3}E(\boldsymbol{r},t). \tag{14}$$

Finally, the corresponding formula for the electromagnetic STOV is found by applying the operator in equation (10). Similarly to the scalar STOV, the result can be written as a vector composed of three components being products of the pulse itself times factors also corresponding to ratios of polynomials comprising in particular the components of the constant vector $\boldsymbol{p}$. Keeping the leading terms in those factors for $k_0 q \gg 1$, we find

$$\mathbf{E}_{\mathrm{STOV}}(\boldsymbol{r},t;\boldsymbol{p}) \approx \frac{2q^7\omega_0^5\left[\pm(ct-z)+\mathrm{i}x\right]}{\mathrm{i}c\,(z-\mathrm{i}q)^8}E(\boldsymbol{r},t)\boldsymbol{p}, \tag{15}$$

where we used the assumption that $\boldsymbol{p}$ was chosen such that $p_z = 0$. Adding the next leading term in the factors multiplying the original pulse introduces first order corrections comprising, on one hand, an additional z-component to the result, and on the other hand an additional contribution to the first two components.

7. Pulses with sagittal skyrmionic distributions

There has been interest recently in the generation of optical analogs [43–47, 59–68] of skyrmions [41, 69–71], which are topological textures in which a spherical parameter space is fully covered in a physical flat (sub)space, according to some rules. This includes pulsed solutions where the electric and magnetic fields cover all directions over transverse planes [72]. A different type of skyrmionic distribution are the so-called full Poincaré beams [42], which are monochromatic paraxial solutions of the wave equation in which all possible states of full polarization are represented in any cross-section of the beam. The spherical parameter space in this case is the Poincaré sphere, whose spherical coordinates,

$$\theta = \arccos\left[\frac{2\mathrm{Im}(E_x^* E_y)}{|E_x|^2+|E_y|^2}\right] \in [-\pi/2,\pi/2] \tag{16a}$$

$$\phi = \arg\left[|E_x|^2-|E_y|^2+2\mathrm{i}\mathrm{Re}(E_x^* E_y)\right] \in [0,2\pi), \tag{16b}$$

characterize the ellipticity/handedness and orientation of the polarization ellipse, respectively. The sphere is mapped onto each transverse plane of these beams according to a stereographical map. Nonparaxial versions of these beams have also been defined [48].

The formulas described in previous sections then suggest that it is possible to create a pulsed distribution of this kind, where polarization is covered not over a transverse plane but over a longitudinal one. The key is to combine an electromagnetic STOV with some choice of $\boldsymbol{p}$ and a copropagating electromagnetic blob with the orthogonal choice of $\boldsymbol{p}$, so that the blob is centered at the STOV's vortex. Here we choose these vectors to give each of these components definite helicity. To make the connection more direct, we consider a pulse close to the paraxial limit ($q = 100c/\omega_0$) and we neglect the electric

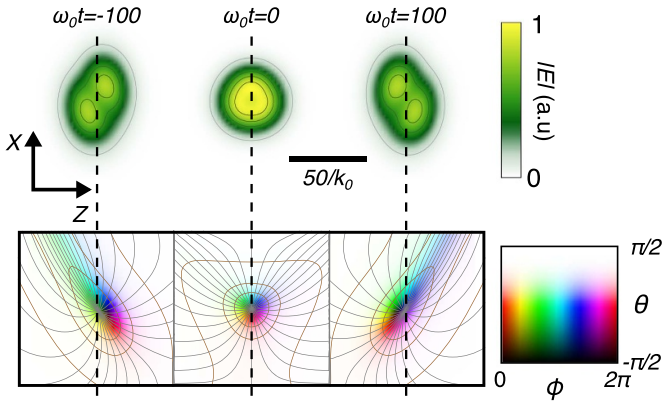

Figure 6. (a), (b) Short-time averaged intensity and (c), (d) transverse polarization distribution for a pulse presenting a sagittal skyrmionic distribution, at (a), (c) $t=0$ and (b), (d) $t=40/\omega_0$. In (c), (d) the outermost visible θ contour corresponds to $\theta=-\frac{7\pi}{16}$.

vector's z component in the calculation of the Stokes parameters. The resulting pulse can then be written as

$$\mathbf{E}_{\text{skyrm}}(\boldsymbol{r},t;\boldsymbol{p}_1,\boldsymbol{p}_2)=\left(\cos\eta\widehat{\mathbf{V}}_{\boldsymbol{p}_1}\widehat{W}+\sin\eta\widehat{\mathbf{V}}_{\boldsymbol{p}_2}\right)E(\boldsymbol{r},t), \quad (17)$$

where $\boldsymbol{p}_1$ and $\boldsymbol{p}_2$ are two mutually orthogonal polarization vectors, and η is a parameter that regulates the polarization state distribution across the pulse's xz section.

These solutions have then the property of presenting essentially all transverse polarization states represented within the sagittal plane $y=0$ (as well as over other nearby planes parallel to this one), normal to the polarization plane. This coverage gets deformed as t departs from the focal time $t=0$. Figure 6 shows the intensity distribution and the polarization state distribution of one of these pulses in the $y=0$ plane, at two propagation instants, for $\boldsymbol{p}_{1,2}$ chosen as $(1,\mp\mathrm{i},0)$ and $\eta=0.76$. It can be observed that almost all full polarization states are represented within the shown region.

8. Concluding remarks

We proposed a method for generating exact solutions of the scalar or (divergence-free) vector wave equations that represent STOVs, valid even for large divergence angles, and obtained the conditions under which these solutions describe a near-circular intensity distribution over a longitudinal plane at the focal time. Several generalizations to these formulas can be considered. First, while we focused on round STOVs, the conditions between the parameters q and s can be relaxed to obtain STOVs with different ellipticities. Also, the coefficients of the operator in equation (5) can be changed and a term proportional to ∂_y can be introduced to tilt the OAM to any arbitrary direction. Higher-order operators can also be considered that induce higher magnitudes of the OAM, although these higher-order vortices would be unstable, disintegrating into simple vortices upon propagation. Finally, the vectorization operator in equation (10) can be chosen differently (as long as it is divergence-free and commutes with the Laplacian), and/or the vector $\boldsymbol{p}$ can be chosen to include significant longitudinal components.

This theoretical model was used to propose variants of STOVs whose transverse field components cover all possible states of paraxial polarization over sagittal planes that are normal to the direction of the OAM. Although we did not calculate it here, the Skyrme density of this polarization coverage does not change sign within the region in which the field is significant and for times near the focal time, so these pulses can be regarded as pulsed optical implementations of Skyrmions.

Data availability statement

No data were generated or analyzed in the presented research.

Acknowledgments

The authors thank Konstantin Bliokh and Etienne Brasselet for useful discussions.

Funding

M A A acknowledges funding from ANR-21-CE24-0014. R G C acknowledges funding from the Labex WIFI (ANR-10-LABX-24, ANR-10-IDEX-0001-02 PSL*).

Conflict of interest

The authors declare no conflicts of interest.

Appendix A. Derivation of the equation for a complex-focus pulse with Poisson-like spectrum

The complex time-dependent field can be calculated as a superposition of monochromatic components according to

$$E(\boldsymbol{r},t)=\int_{-\infty}^{\infty}U(\boldsymbol{r},\omega)\exp(-\mathrm{i}\omega t)\mathrm{d}\omega, \quad (A1)$$

where $U(\boldsymbol{r},\omega)$ satisfies the Helmholtz equation. By substituting the expressions for $U(\boldsymbol{r},\omega)$ in equations (1) and (2), we get

$$\begin{aligned}E(\boldsymbol{r},t)=&\left(\frac{s}{\omega_0}\right)^{s+1}\frac{1}{\Gamma(s+1)R}\\&\times\int_0^{\infty}\omega^{s-1}\left\{\exp\left[\left(-\frac{s}{\omega_0}-\mathrm{i}t_-\right)\omega\right]\right.\\&\left.-\exp\left[\left(-\frac{s}{\omega_0}-\mathrm{i}t_+\right)\omega\right]\right\}\mathrm{d}\omega,\end{aligned} \quad (A2)$$

where $t_\pm=t\pm R/c-\mathrm{i}q/c$. Note that ω^{s-1} can be replaced by $(\mathrm{i}\partial/\partial t)^{s-1}$, which can be extracted from the integral. The remaining integrals are then straightforward to evaluate, as are the derivatives of the result, leading to equation (3).

Appendix B. Dimensions of the wave packet and condition to make it round

We now carry out an asymptotic analysis to obtain the conditions under which the blob-like wave packet in equation (3) has a round shape at $t = 0$. The first step is to look at the focal point to see that one of the two terms in the expression dominates, which will simplify the derivation that will follow. Setting all arguments to zero we find

$$E(\mathbf{0},0) = \frac{1}{-\mathrm{i}\omega_0 q}\left[1 - \frac{1}{\left(1+\frac{2\omega_0 q}{sc}\right)^s}\right]. \tag{B1}$$

We see that for large s the first term (involving t_-) dominates. We then use in the derivations in this section the following approximation:

$$E(\mathbf{r},t) \approx \frac{1}{\omega_0 R\left(1+\mathrm{i}\frac{\omega_0}{s}t_-\right)^s}. \tag{B2}$$

Let us now study the extension of the wave packet in the transverse and longitudinal directions, to find conditions for the curvatures of the intensity to match. We start with the transverse profile. As x and y are interchangeable, we choose to work with the x-coordinate. Thus, setting y, z and t equal to zero, and ignoring the contribution involving t_+, the field is found to be approximately equal to

$$E(x\widehat{\mathbf{x}},0) \approx \frac{1}{\omega_0\sqrt{x^2-q^2}}\frac{1}{\left[1-\mathrm{i}\frac{\omega_0}{cs}\left(\sqrt{x^2-q^2}+\mathrm{i}q\right)\right]^s}. \tag{B3}$$

We study this expression in the focal region, so we assume that x^2 is much smaller than q^2 and we can approximate $\sqrt{x^2-q^2}$ as $-\mathrm{i}q(1-x^2/2q^2)$. The field's expression becomes

$$\begin{aligned} E(x\widehat{\mathbf{x}},0) &\approx \frac{1}{-\mathrm{i}\omega_0 q\left(1-\frac{x^2}{2q^2}\right)}\frac{1}{\left(1+\frac{\omega_0}{2csq}x^2\right)^s} \\ &\approx -\frac{1}{\mathrm{i}\omega_0 q}\left(1+\frac{x^2}{2q^2}\right)\frac{1}{\left(1+\frac{\omega_0}{2scq}x^2\right)^s}. \end{aligned} \tag{B4}$$

The short-time-averaged intensity along the x-axis is approximately given by

$$\begin{aligned} I(x\widehat{\mathbf{x}},0) &= |E(x\widehat{\mathbf{x}},0)|^2 \\ &\approx \frac{1}{\omega_0^2 q^2}\left(1+\frac{x^2}{2q^2}\right)^2\frac{1}{\left(1+\frac{\omega_0}{2scq}x^2\right)^{2s}} \\ &\approx \frac{1}{\omega_0^2 q^2}\left(1+\frac{x^2}{q^2}\right)\left[1-(2s)\frac{\omega_0}{2scq}x^2\right] \\ &\approx \frac{1}{\omega_0^2 q^2}\left(1-C_\perp x^2\right) \\ &\approx \frac{\exp\left(-C_\perp x^2\right)}{\omega_0^2 q^2}, \end{aligned} \tag{B5, B6}$$

where $C_\perp$ is given by

$$C_\perp = \frac{\omega_0}{cq} - \frac{1}{q^2}. \tag{B7}$$

Note that $C_\perp^{-1/2}$ is a measure of the extent in the transverse direction of the pulse's envelope.

We now look at the longitudinal profile. Setting x, y and t to zero, the field is approximately equal to

$$E(z\widehat{\mathbf{z}},0) \approx \frac{1}{\omega_0(z-\mathrm{i}q)}\frac{1}{\left(1-\frac{\mathrm{i}\omega_0}{s}\frac{z}{c}\right)^s}. \tag{B8}$$

By assuming $|z| \ll q$, and keeping the terms up to second order in z, the short-time average intensity along the z-axis near the origin is seen to be given approximately by

$$\begin{aligned} I(z\widehat{\mathbf{z}},0) &\approx |E(z\widehat{\mathbf{z}},0)|^2 \\ &\approx \frac{1}{\omega_0^2 q^2}\left(1-C_z z^2\right) \\ &\approx \frac{\exp\left(-C_z z^2\right)}{\omega_0^2 q^2}, \end{aligned} \tag{B9}$$

with

$$C_z = \frac{1}{s}\frac{\omega_0^2}{c^2} + \frac{1}{q^2}. \tag{B10}$$

Here, $C_z^{-1/2}$ is an approximate measure of the length of the envelope of the pulse in the longitudinal direction.

To ensure the roundness of the wave packet, the lengths in the transverse and longitudinal directions need to be equal, so that

$$C_\perp = C_z \qquad \Leftrightarrow \qquad s = \frac{k_0^2 q^2}{k_0 q - 2}, \tag{B11}$$

with $k_0 = \omega_0/c$. Note that for the complex focus method to lead to solutions that resemble beams or pulses propagating towards larger z, one must make the assumption that q is considerably larger than the wavelength for the central frequency ω_0, since otherwise a non-negligible amount of counter-propagating plane wave components would be present. We therefore consider the case in which $k_0 q$ is sufficiently large compared to unity, and we obtain the simple approximate result in equation (5), where the second term is an order below the first and hence could be ignored, but we keep it as a first correction given its simplicity.

Appendix C. Condition to obtain a round scalar STOV

Let us propose a differential operator of the form

$$\widehat{W} = \frac{c}{\omega_0}\partial_x + \mathrm{i}\left(\alpha\frac{1}{\omega_0}\partial_t + \beta\frac{c}{\omega_0}\partial_z + \mathrm{i}\gamma\right). \tag{C1}$$

We now find values for the parameters α, β and γ that produce a round STOV when applying this operator to the pulse

discussed in the previous two sections. For this, we apply this operator to the approximate form in equation (B2). Let us look at each derivative separately:

$$\partial_x E(\boldsymbol{r},t) \approx -\frac{x}{R}\left(\frac{1}{R}+\mathrm{i}\frac{\omega_0}{c}\frac{1}{1+\mathrm{i}\frac{\omega_0}{s}t_-}\right)E(\boldsymbol{r},t), \tag{C2a}$$

$$\partial_z E(\boldsymbol{r},t) \approx -\frac{z-\mathrm{i}q}{R}\left(\frac{1}{R}+\mathrm{i}\frac{\omega_0}{c}\frac{1}{1+\mathrm{i}\frac{\omega_0}{s}t_-}\right)E(\boldsymbol{r},t), \tag{C2b}$$

$$\partial_t E(\boldsymbol{r},t) \approx -\mathrm{i}\frac{\omega_0}{1+\mathrm{i}\frac{\omega_0}{s}t_-}E(\boldsymbol{r},t) \tag{C2c}$$

where we used $\partial_x R = x/R$ and $\partial_z R = (z-\mathrm{i}q)/R$. For simplifying the derivation, we work with the quantity $\widehat{W}E/E$, which gives

$$\frac{\widehat{W}E(\boldsymbol{r},t)}{E(\boldsymbol{r},t)} \approx -\frac{c}{\omega_0}\frac{x}{R^2}+\mathrm{i}\frac{x}{R\left(1+\mathrm{i}\frac{\omega_0}{s}t_-\right)}+\alpha\frac{1}{\left(1+\mathrm{i}\frac{\omega_0}{s}t_-\right)} +\mathrm{i}\beta\left[-\frac{c}{\omega_0}\frac{z-\mathrm{i}q}{R^2}+\mathrm{i}\frac{(z-\mathrm{i}q)}{R\left(1+\mathrm{i}\frac{\omega_0}{s}t_-\right)}\right]-\gamma. \tag{C3}$$

Ideally, for $y=ct=0$ this factor should take the form of a vortex in the xz plane centered at the origin. To simplify this expression, we now use expanded expressions of the factors $1/(1+\mathrm{i}\omega_0 t_-/s)$, $1/R$ and $1/R^2$ up to second order in x and z, assuming large values of q. We fix $y=ct=0$, and to ensure that we use the appropriate root for the term we are using we write $R=-\mathrm{i}\sqrt{(q+\mathrm{i}z)^2-x^2}$. The obtained expansions are as follows:

$$\left(1+\mathrm{i}\frac{\omega_0}{s}t_-\right)^n \approx 1-\mathrm{i}\frac{n\omega_0 z}{cs}+n\omega_0\frac{csx^2+(1-n)q\omega_0 z^2}{2c^2s^2q}, \tag{C4a}$$

$$R^n \approx (-\mathrm{i}q)^n\left[1+\mathrm{i}n\frac{z}{q}-n\frac{x^2+(n-1)z^2}{2q^2}\right]. \tag{C4b}$$

Using these results in equation (C3) evaluated at $y=ct=0$, and keeping the terms up to second order in x and z, we obtain:

$$\frac{\widehat{W}E(x\hat{\mathbf{x}}+z\hat{\mathbf{z}},0)}{E(x\hat{\mathbf{x}}+z\hat{\mathbf{z}},0)} \approx K_0+K_x x+\mathrm{i}K_z z+K_{xx}x^2+\mathrm{i}K_{xz}xz+K_{zz}z^2, \tag{C5}$$

where K_0, K_x, K_z, K_{xx}, K_{xz} and K_{zz} are the following real constants:

$$K_0 = \beta\frac{c}{q\omega_0}-\gamma+(\alpha-\beta), \tag{C6a}$$

$$K_x = \frac{c-q\omega_0}{q^2\omega_0}, \tag{C6b}$$

$$K_z = -\frac{\beta c}{q^2\omega_0}+\frac{(\alpha-\beta)\omega_0}{cs}, \tag{C6c}$$

$$K_{xx} = -\frac{\beta}{2q^2}+\frac{\beta c}{q^3\omega_0}+(\beta-\alpha)\frac{\omega_0}{2csq}, \tag{C6d}$$

$$K_{xz} = \frac{1}{q^2}-\frac{2c}{q^3\omega_0}-\frac{\omega_0}{cqs}, \tag{C6e}$$

$$K_{zz} = (\beta-\alpha)\frac{\omega_0^2}{c^2s^2}-\frac{\beta c}{\omega_0 q^3}. \tag{C6f}$$

To solve for α, β and γ, we need to find three equations in terms of these five coefficients. Having an isotropic vortex at the origin imposes the first two conditions:

$$K_0 = 0, \tag{C7a}$$

$$K_x = \pm K_z. \tag{C7b}$$

A nicely symmetric vortex would ideally also require that the remaining coefficients vanish. However, it is not possible to simultaneously satisfy the resulting five constraints. Therefore, to find the best possible third constraint, we first change to polar coordinates according to $x=r\sin\varphi$ and $z=r\cos\varphi$, so that equation (C5) can then be rewritten as

$$\frac{\widehat{W}E(x\hat{\mathbf{x}}+z\hat{\mathbf{z}},0)}{E(x\hat{\mathbf{x}}+z\hat{\mathbf{z}},0)} \approx \mathrm{i}K_z r\exp(\pm\mathrm{i}\varphi) +r^2\left[B+C_+\exp(2\mathrm{i}\varphi)+C_-\exp(-2\mathrm{i}\varphi)\right], \tag{C8}$$

where

$$B = \frac{K_{xx}+K_{zz}}{2}, \tag{C9a}$$

$$C_\pm = \frac{K_{zz}-K_{xx}\pm K_{xz}}{4}. \tag{C9b}$$

The modulus squared of this expression gives

$$\left|\frac{\widehat{W}E(x\hat{\mathbf{x}}+z\hat{\mathbf{z}},0)}{E(x\hat{\mathbf{x}}+z\hat{\mathbf{z}},0)}\right|^2 \approx K_z^2 r^2 -2K_z r^3\left[(C_\pm-B)\sin\varphi+C_\mp\sin 3\varphi\right]. \tag{C10}$$

The term that disrupts the most the roundness of the resulting intensity pattern is that proportional to $\sin\varphi$. Therefore, depending on the choice of vorticity, corresponding to the choice of sign in equation (C7*b*), we impose the condition $C_\pm = B$, which gives

$$3K_{xx}+K_{zz} = \pm K_{xz}. \tag{C11}$$

Equations (C7*a*), (C7*b*) and (C11) then form a system that can be solved to obtain the solutions for α, β and γ. For the top choice of the sign, these solutions are:

$$\alpha = -\frac{5c^3s^2+3c^2q\omega_0 s(1-s)-cq^2\omega_0^2(2-s)+4q^3\omega_0^3}{cq\omega_0(cs-2q\omega_0-3qs\omega_0)}, \tag{C12a}$$

$$\beta = -\frac{c^2s-2cq\omega_0+cqs\omega_0+4q^2\omega_0^2}{c(cs-2q\omega_0-3qs\omega_0)}, \tag{C12b}$$

$$\gamma = \frac{c^2s+5c^2s^2-2cq\omega_0+3cqs\omega_0-3cqs^2\omega_0+4q^2\omega_0^2}{q\omega_0(-cs+2q\omega_0+3qs\omega_0)}. \tag{C12c}$$

which can be approximated, using $s\approx k_0 q$ by:

$$\alpha \approx \frac{2}{3}-\frac{26}{9s}, \qquad \beta \approx \frac{5}{3}-\frac{32}{9s}, \qquad \gamma \approx -1+\frac{7}{3s}. \tag{C13}$$

Appendix D. Condition to obtain a round vector STOV

To find the parameters that make a round vector STOV, we consider the short-time-averaged intensity

$$I(\boldsymbol{r},t) = |\mathbf{E}_{\mathrm{STOV}}(\boldsymbol{r},t;\boldsymbol{p})|^2. \tag{D1}$$

As was done in appendix C, we evaluate the resulting expression at $ct = y = 0$ and express x and z in polar coordinates. However, it turns out that a rounder short-time-averaged intensity profile is achieved if we allow for a small lateral displacement of magnitude x_0 for the intensity minimum away from the origin; we therefore write $x = x_0 + r\sin\varphi$ and $z = r\cos\varphi$, and separate the result in terms of powers of r. We can then impose a series of constraints:

(i) that the intensity at the center (the part that is independent of r) be zero or as small as possible;
(ii) that the part of the intensity linear in r (which happens to also be proportional to $\sin\varphi$) be zero;
(iii) that the coefficient of r^2 be independent of φ; and
(iv) that the part of the coefficient of r^3 that oscillates as $\sin\varphi$ be zero (the remaining part oscillating as $\sin 3\varphi$).

The idea is to use these four constraints to determine α, β, γ and x_0. The expressions for these constraints are long and difficult to solve. To simplify the solution, we first consider the leading terms of the constraints in the limit of large q. By using computer algebra, we show that constraints (i), (ii) and (iv) all give the same relation to leading order:

$$\beta + \gamma - \alpha = \mathcal{O}\left(q^{-1}\right), \tag{D2a}$$

while constraint (iii) gives, once this prior constraint is taken into account,

$$\beta = \alpha \pm 1 + \mathcal{O}\left(q^{-1}\right), \qquad \gamma = \mp 1 + \mathcal{O}\left(q^{-1}\right). \tag{D2b}$$

Let us choose the top choice for the sign (the other choice would just reverse the sign of the orbital angular momentum.) We then look at the next order corrections for α, β, and γ, by looking at the corresponding corrections for the four constraints. It turns out that constraint (iii) has two parts, one independent of $\boldsymbol{p}$ and one that depends on this choice; the first part cannot be fully satisfied, so we only use the second in combination with the remaining constraints. We then find that the lateral displacement of the center is $x_0 = -1/(7k_0)$, namely a small fraction of the main wavelength, and the coefficients are given by

$$\alpha = \frac{6}{7} + \left(\kappa + \frac{237}{98}\right)\frac{c}{\omega_0 q}, \tag{D3a}$$

$$\beta = \frac{13}{7} + \kappa\frac{c}{\omega_0 q}, \tag{D3b}$$

$$\gamma = -1 + \frac{237}{98}\frac{c}{\omega_0 q}, \tag{D3c}$$

where the constant κ is a correction that is not fixed by the constraints. Numerical tests for small q show that the STOV remains fairly round if this free constant is chosen to eliminate the correction to α. The coefficients are then, when written in terms of s

$$\alpha = \frac{6}{7}, \qquad \beta = \frac{13}{7} - \frac{237}{98s}, \qquad \gamma = -1 + \frac{237}{98s}. \tag{D4}$$

Appendix E. Paraxial limit

We now give the derivation for obtaining the limiting expression of the pulse when approaching the paraxial regime. We start from the approximate expression in equation (B2), which we write as

$$E(\boldsymbol{r},t) \approx \frac{1}{\omega_0 R}\left(1 + \mathrm{i}\frac{\omega_0}{s}t_-\right)^{-s}, \tag{E1}$$

where we recall that $R = \sqrt{\rho^2 + (z - \mathrm{i}q)^2}$ with $\rho^2 = x^2 + y^2$, and $t_- = t - R/c - \mathrm{i}q/c$.

Since, in the paraxial regime, the pulse tends to a Gaussian, we aim at transforming equation (E1) into an expression comprising an exponential. More specifically, we are looking for a correspondence between expansions up to second order of, on the one hand, an expression of the form $(1+\epsilon)^{-N}$ and, on the other hand, an exponential of the form $[\exp(\epsilon + \varphi)]^{-N}$, where $|\epsilon|$ is a small quantity and φ is introduced in the exponential as a possible correction term. We start by considering the expansion of both expressions up to second order:

$$(1+\epsilon)^{-N} \approx 1 - N\epsilon + \frac{N(N+1)}{2}\epsilon^2, \tag{E2a}$$

and

$$\begin{aligned}[\exp(\epsilon+\mu)]^{-N} &\approx 1 - N(\epsilon+\mu) + \frac{N^2}{2}(\epsilon+\mu)^2 \\ &\approx 1 - N\epsilon - N\mu + \frac{N^2}{2}\epsilon^2,\end{aligned} \tag{E2b}$$

where we assumed that $|\mu|$ is much smaller than $|\epsilon|$, so we can neglect the terms in higher orders of μ or products of μ with ϵ. Therefore, by equating equations (E2a) and (E2b), we find that μ must be chosen as

$$\mu = -\frac{\epsilon^2}{2}, \tag{E3}$$

so that

$$(1+\epsilon)^{-N} \approx \exp\left(-N\epsilon + N\frac{\epsilon^2}{2}\right). \tag{E4}$$

Using this result, we can write an approximation for equation (E1) valid for small $|\omega_0 t_-/c|$ as

$$E(\boldsymbol{r},t) \approx \frac{1}{\omega_0 R}\exp\left(-\mathrm{i}\omega_0 t_- - \frac{\omega_0^2 t_-^2}{2s}\right). \tag{E5}$$

The expansion of R is the paraxial regime is given by:

$$R \approx z - \mathrm{i}q + \frac{\rho^2}{2\,(z - \mathrm{i}q)}. \tag{E6}$$

We can then write t_- as

$$t_- \approx t - \frac{z}{c} - \frac{\rho^2}{2c\,(z - \mathrm{i}q)}. \tag{E7}$$

As is well known, while the paraxial approximation requires keeping terms of up to second order in the transverse variable in the exponent, a zeroth order approximation suffices for the amplitude, so we can approximate the prefactor $1/R$ as $1/(z - \mathrm{i}q)$ in equation (E5). Finally, using the condition for making the pulse round, $\omega_0/sc \approx 1/q$, we get the expression in equation (13).

ORCID iDs

R Gutiérrez-Cuevas https://orcid.org/0000-0002-3451-6684
M A Alonso https://orcid.org/0000-0001-7037-5383

References

[1] Hernández-Figueroa H E, Zamboni-Rached M and Recami E 2008 *Localized Waves* vol 194 (Wiley)
[2] Turunen J and Friberg A T 2010 Propagation-invariant optical fields *Progress in Optics* vol 54 (Elsevier) pp 1–88
[3] Yessenov M, Hall L A, Schepler K L and Abouraddy A F 2022 Space-time wave packets *Adv. Opt. Photon.* **14** 455–570
[4] Hellwarth R W and Nouchi P 1996 Focused one-cycle electromagnetic pulses *Phys. Rev.* E **54** 889–95
[5] Zdagkas A, Papasimakis N, Savinov V, Dennis M R and Zheludev N I 2019 Singularities in the flying electromagnetic doughnuts *Proc. SPIE* **8** 1379–85
[6] Zdagkas A, McDonnell C, Deng J, Shen Y, Li G, Ellenbogen T, Papasimakis N and Zheludev N I 2022 Observation of toroidal pulses of light *Nat. Photon.* **16** 523–8
[7] Dror N and Malomed B A 2011 Symmetric and asymmetric solitons and vortices in linearly coupled two-dimensional waveguides with the cubic-quintic nonlinearity *Physica* D **240** 526–41
[8] Sukhorukov A P and Yangirova V V 2005 Spatio-temporal vortices: properties, generation and recording *Nonlinear Optics Applications* ed M A Karpierz, A D Boardman and G I Stegeman (SPIE)
[9] Bliokh K Y and Nori F 2012 Spatiotemporal vortex beams and angular momentum *Phys. Rev.* A **86** 033824
[10] Jhajj N, Larkin I, Rosenthal E W, Zahedpour S, Wahlstrand J K and Milchberg H M 2016 Spatiotemporal optical vortices *Phys. Rev.* X **6** 031037
[11] Hancock S W, Zahedpour S, Goffin A and Milchberg H M 2019 Free-space propagation of spatiotemporal optical vortices *Optica* **6** 1547
[12] Chong A, Wan C, Chen J and Zhan Q 2020 Generation of spatiotemporal optical vortices with controllable transverse orbital angular momentum *Nat. Photon.* **14** 350–4
[13] Hancock S W, Zahedpour S and Milchberg H M 2021 Second-harmonic generation of spatiotemporal optical vortices and conservation of orbital angular momentum *Optica* **8** 594–7
[14] Hancock S W, Zahedpour S and Milchberg H M 2021 Mode structure and orbital angular momentum of spatiotemporal optical vortex pulses *Phys. Rev. Lett.* **127** 193901
[15] Huang S, Wang P, Shen X and Liu J 2021 Properties of the generation and propagation of spatiotemporal optical vortices *Opt. Express* **29** 26995–7003
[16] Bliokh K Y 2021 Spatiotemporal vortex pulses: angular momenta and spin-orbit interaction *Phys. Rev. Lett.* **126** 243601
[17] Mazanov M, Sugic D, Alonso M A, Nori F and Bliokh K Y 2021 Transverse shifts and time delays of spatiotemporal vortex pulses reflected and refracted at a planar interface *Proc. SPIE* **11** 737–44
[18] Wan C, Chen J, Chong A and Zhan Q 2022 Photonic orbital angular momentum with controllable orientation *Natl. Sci. Rev.* **9** nwab149
[19] Porras M A 2023 Transverse orbital angular momentum of spatiotemporal optical vortices *Prog. Electromagn. Res.* **177** 95–105
[20] Bliokh K Y 2023 Orbital angular momentum of optical, acoustic and quantum-mechanical spatiotemporal vortex pulses *Phys. Rev.* A **107** L031501
[21] Porras M A 2024 Clarification of the transverse orbital angular momentum of spatiotemporal optical vortices *J. Opt.* **26** 095601
[22] Bekshaev A 2024 Spatio-temporal optical vortices: principles of description and basic properties (arXiv:2403.01751)
[23] Abramochkin E G and Volostnikov V G 2004 Generalized gaussian beams *J. Opt. A: Pure Appl. Opt.* **6** S157
[24] Gutiérrez-Cuevas R, Dennis M R and Alonso M A 2019 Generalized Gaussian beams in terms of jones vectors *J. Opt.* **21** 084001
[25] Berry M V 1994 Evanescent and real waves in quantum billiards and Gaussian beams *J. Phys. A: Math. Gen.* **27** L391–8
[26] Sheppard C J R and Saghafi S 1998 Beam modes beyond the paraxial approximation: a scalar treatment *Phys. Rev.* A **57** 2971–9
[27] Sheppard C J R and Saghafi S 1999 Electromagnetic Gaussian beams beyond the paraxial approximation *J. Opt. Soc. Am.* A **16** 1381
[28] Moore N J and Alonso M A 2009 Closed-form bases for the description of monochromatic, strongly focused, electromagnetic fields *J. Opt. Soc. Am.* A **26** 2211
[29] Moore N J and Alonso M A 2009 Bases for the description of monochromatic, strongly focused, scalar fields *J. Opt. Soc. Am.* A **26** 1754
[30] Gutiérrez-Cuevas R and Alonso M A 2017 Scalar and electromagnetic nonparaxial bases composed as superpositions of simple vortex fields with complex foci *Opt. Express* **25** 14856
[31] Moore N J and Alonso M A 2008 Closed form formula for Mie scattering of nonparaxial analogues of Gaussian beams *Opt. Express* **16** 5926–33
[32] Gutiérrez-Cuevas R, Moore N J and Alonso M A 2018 Lorenz-Mie scattering of focused light via complex focus fields: an analytic treatment *Phys. Rev.* A **97** 053848
[33] Heyman E and Felsen L 1986 Propagating pulsed beam solutions by complex source parameter substitution *IEEE Trans. Antennas Propag.* **34** 1062–5
[34] Heyman E and Felsen L B 1989 Complex-source pulsed-beam fields *J. Opt. Soc. Am.* A **6** 806
[35] Heyman E and Felsen L B 2001 Gaussian beam and pulsed-beam dynamics: complex-source and complex-spectrum formulations within and beyond paraxial asymptotics *J. Opt. Soc. Am.* A **18** 1588–611
[36] Saari P 2001 Evolution of subcycle pulses in nonparaxial Gaussian beams *Opt. Express* **8** 590

[37] Lin Q, Zheng J and Becker W 2006 Subcycle pulsed focused vector beams *Phys. Rev. Lett.* **97** 253902
[38] April A 2010 Ultrashort, strongly focused laser pulses in free space *Coherence and Ultrashort Pulse Laser Emission* (InTech)
[39] Porras M A 1998 Ultrashort pulsed Gaussian light beams *Phys. Rev.* E **58** 1086
[40] Caron C F R and Potvliege R M 1999 Free-space propagation of ultrashort pulses: space-time couplings in Gaussian pulse beams *J. Mod. Opt.* **46** 1881–91
[41] Skyrme T H R 1961 A non-linear field theory *Proc. R. Soc.* A **260** 127–38
[42] Beckley A M, Brown T G and Alonso M A 2010 Full Poincaré beams *Opt. Express* **18** 10777–85
[43] Tsesses S, Ostrovsky E, Cohen K, Gjonaj B, Lindner N H and Bartal G 2018 Optical skyrmion lattice in evanescent electromagnetic fields *Science* **361** 993–6
[44] Du L, Yang A, Zayats A V and Yuan X 2019 Deep-subwavelength features of photonic skyrmions in a confined electromagnetic field with orbital angular momentum *Nat. Phys.* **15** 650–4
[45] Gutiérrez-Cuevas R and Pisanty E 2021 Optical polarization skyrmionic fields in free space *J. Opt.* **23** 024004
[46] Gao S, Speirits F C, Castellucci F, Franke-Arnold S, Barnett S M and Götte J B 2020 Paraxial skyrmionic beams *Phys. Rev.* A **102** 053513
[47] Sugic D, Droop R, Otte E, Ehrmanntraut D, Nori F, Ruostekoski J, Denz C and Dennis M R 2021 Particle-like topologies in light *Nat. Commun.* **12** 6785
[48] Gutiérrez-Cuevas R and Alonso M A 2021 Analytic treatment of nonparaxial full-Poincaré fields: singularity structure and trapping properties *J. Opt.* **23** 024005
[49] Wang Z, Zhang Z, Xu Z and Lin Q 1997 Space-time profiles of an ultrashort pulsed Gaussian beam *IEEE J. Quantum Electron.* **33** 566–73
[50] Feng S and Winful H G 2000 Spatiotemporal structure of isodiffracting ultrashort electromagnetic pulses *Phys. Rev.* E **61** 862–73
[51] Berry M V and McDonald K T 2008 Exact and geometrical optics energy trajectories in twisted beams *J. Opt. A: Pure Appl. Opt.* **10** 035005
[52] Alonso M A and Dennis M R 2017 Ray-optical Poincaré sphere for structured gaussian beams *Optica* **4** 476–86
[53] Landesman B T and Barrett H H 1988 Gaussian amplitude functions that are exact solutions to the scalar Helmholtz equation *J. Opt. Soc. Am.* A **5** 1610
[54] Sheppard C J R 2000 Polarization of almost-plane waves *J. Opt. Soc. Am.* A **17** 335
[55] Alonso M A 2011 The effect of orbital angular momentum and helicity in the uncertainty-type relations between focal spot size and angular spread *J. Opt.* **13** 064016
[56] Bliokh K Y, Alonso M A, Ostrovskaya E A and Aiello A 2010 Angular momenta and spin-orbit interaction of nonparaxial light in free space *Phys. Rev.* A **82** 063825
[57] Bliokh K Y and Aiello A 2013 Goos-Hänchen and Imbert-Fedorov beam shifts: an overview *J. Opt.* **15** 014001
[58] Bliokh K Y, Rodríguez-Fortuño F J, Nori F and Zayats A V 2015 Spin–orbit interactions of light *Nat. Photon.* **9** 796–808
[59] Donati S, Dominici L, Dagvadorj G, Ballarini D, De Giorgi M, Bramati A, Gigli G, Rubo Y G, Szymańska M H and Sanvitto D 2016 Twist of generalized skyrmions and spin vortices in a polariton superfluid *Proc. Natl. Acad. Sci.* **113** 14926–31
[60] Lei X, Yang A, Shi P, Xie Z, Du L, Zayats A V and Yuan X 2021 Photonic spin lattices: symmetry constraints for skyrmion and meron topologies *Phys. Rev. Lett.* **127** 237403
[61] Ghosh A, Yang S, Dai Y, Zhou Z, Wang T, Huang C-B and Petek H 2021 A topological lattice of plasmonic merons *Appl. Phys. Rev.* **8** 041413
[62] Shen Y 2021 Topological bimeronic beams *Opt. Lett.* **46** 3737–40
[63] Shen Y, Zhang Q, Shi P, Du L, Zayats A V and Yuan X 2022 Topological quasiparticles of light: optical skyrmions and beyond (arXiv:2205.10329)
[64] Zhang Q, Xie Z, Shi P, Yang H, He H, Du L and Yuan X 2022 Optical topological lattices of Bloch-type skyrmion and meron topologies *Photonics Res.* **10** 947–57
[65] Berškys J and Orlov S 2023 Accelerating Airy beams with particle-like polarization topologies and free-space bimeronic lattices *Opt. Lett.* **48** 1168–71
[66] Marco D, Herrera I, Brasselet S and Alonso M A 2023 Periodic skyrmionic textures via conformal cartographic projections (arXiv:2310.08964)
[67] Ghosh A, Yang S, Dai Y and Petek H 2023 The spin texture topology of polygonal plasmon fields *ACS Photonics* **10** 13–23
[68] Marco D and Alonso M A 2022 Optical fields spanning the 4D space of nonparaxial polarization (arXiv:2212.01366)
[69] Nagaosa N and Tokura Y 2013 Topological properties and dynamics of magnetic skyrmions *Nat. Nanotechnol.* **8** 899–911
[70] Manton N S 1987 Geometry of skyrmions *Commun. Math. Phys.* **111** 469–78
[71] Esteban M J 1986 A direct variational approach to Skyrme's model for meson fields *Commun. Math. Phys.* **105** 571–91
[72] Shen Y, Hou Y, Papasimakis N and Zheludev N I 2021 Supertoroidal light pulses as electromagnetic skyrmions propagating in free space *Nat. Commun.* **12** 5891